Production of hadrons at large transverse momentum at 200, 300, and 400 GeV *

J. W. Cronin, H. J. Frisch, and M. J. Shochet

The Enrico Fermi Institute, University of Chicago, Chicago, Illinois 60637

J. P. Boymond, P. A. Piroué, and R. L. Sumner

Department of Physics, Joseph Henry Laboratories, Princeton University, Princeton, New Jersey 08540

(Received 5 December 1974)

We have measured, as a function of transverse momentum $(p_\perp)$, the invariant cross section $E d\sigma/d^3 p$ for the production of $\pi^\pm$, $K^\pm$, p, $\bar{p}$, d, and $\bar{d}$ in proton collisions with a tungsten (W) target at incident proton energies of 200, 300, and 400 GeV. The measurements were made in the region of 90° in the c.m. system of the incident proton and a single nucleon at rest. Measurements were also made with 300-GeV protons incident on Be, Ti, and W targets of equal interaction length. These p-nucleus measurements, which show a strong dependence on atomic number at high $p_\perp$, were used to extract effective proton-nucleon cross sections by extrapolation to atomic number unity. At large values of the scaling variable $x_\perp = 2 p_\perp /\sqrt{s}$, where s is the square of the c.m. energy, the pion data are found to be well represented by the expression $(\sqrt{s})^{-n} e^{-a x_\perp}$, with $n = 11.0 \pm 0.4$ and $a = 36.0 \pm 0.4$. At $x_\perp < 0.35$, where similar measurements have been made at the CERN ISR, our data are in good agreement with the ISR data.

I. INTRODUCTION

In this paper we present results from a study of particle production at large transverse momentum $(p_\perp)$ carried out at the Fermi National Accelerator Laboratory (Fermilab). This experiment was performed in several runs during a 9-month period. We were originally motivated by the simple notion that the observation of large $p_\perp$ events may correspond to collisions at short distances. (A $p_\perp$ of 6 GeV/c corresponds to a distance $d \approx \hbar/p_\perp \approx 3 \times 10^{-15}$ cm.) In collisions at short distances, one might expect new phenomena to appear. Therefore, we prepared an apparatus to observe the production of long-lived charged particles by 200–400-GeV protons incident on nuclear targets. The apparatus was designed to detect charged hadrons, muons, and electrons. The production angle of 77 mrad was chosen because it corresponds to $\sim 90°$ in the c.m. system for the production of a relativistic particle by a 300-GeV proton incident on a proton at rest. We present here results of our studies of hadron production.

Experimentally, it had been known[1] for some time that the $p_\perp$ distributions of long-lived particles produced in high-energy hadron collisions were falling off exponentially $(e^{-b p_\perp})$, with the average transverse momentum $\langle p_\perp \rangle = 0.3 - 0.5$ GeV/c, approximately independent of both the secondary particle energy E and the c.m. energy $\sqrt{s}$ of the collision. Recent measurements[2] at the CERN Intersecting Storage Rings (ISR) have in general confirmed these values of $\langle p_\perp \rangle$. However, at high $p_\perp$ (>3 GeV/c), a much more copious pion

production has been observed[3–5] than predicted by the extrapolation of the data at small $p_\perp$ (<1 GeV/c).

Theoretical papers by Berman, Bjorken, and Kogut[6] and Blankenbecler, Brodsky, and Gunion[7] emphasized the possible relevance of hadron production at high $p_\perp$ to the investigation of the constituent nature of the nucleon. In recent years the theoretical literature on this topic has increased enormously.[8]

In the next section we describe the experimental arrangement used in this investigation. In Sec. III we discuss the acquisition of the data, and in Sec. IV, their reduction. In Sec. V we present the results. We discuss the derivation of the cross sections on a free nucleon from our measurements on nuclei in Sec. VI. These cross sections are compared with similar measurements made at the CERN ISR and with general theoretical predictions. In Sec. VII a summary and conclusions are presented.

II. EXPERIMENTAL ARRANGEMENT

A. Beam and targets

The experiment was performed in an external proton beam of the Fermilab which was directed to the Proton Area. Within the Proton Area the beam can be directed to any of three experimental pits. Our experiment was set up in the pit designated Proton East. For the later runs of this experiment, a beam-splitting station was installed. With the splitting station the fraction of the beam directed to Proton East could easily be varied

from 1% to 100% of that directed to the entire Proton Area. This flexibility in beam intensity was important since the cross sections we measured varied by more than 10 orders of magnitude over the range of $p_\perp$ studied.

The proton beam was focused to a spot ~2 mm in diameter. The targets, mounted on a movable stage, could be remotely positioned. The beam could also be positioned with the aid of steering magnets.

The incident beam intensity was monitored by a secondary emission monitor (SEM). The SEM was calibrated radiochemically. The reproducibility of the calibration was ~15%, and the absolute calibration is estimated to have a precision of ±25%.

The proton interactions in the target were monitored by two separate scintillation counter telescopes placed at 90° to the incident protons. At the production target the proton beam is 14 ft below the surface, in a tunnel. The monitors observed charged particles from the target through a vertical shaft. The particles were required to traverse the 15-in.-thick concrete roof of the tunnel before striking the monitor telescope. When the beam was properly positioned on the target, the ratio of the rate in each scintillation telescope to the SEM was stable to better than ±5%.

The study of hadron production at large $p_\perp$ was divided into two separate parts. First, data were taken with 200-, 300-, and 400-GeV protons incident on a $\frac{1}{8}$-in.-diam by 2-in.-long W target. Second, data were taken with 300-GeV protons incident on targets of Be, Ti, and W. These targets were chosen to have the same nuclear inelastic interaction length.[9] In each target 20% of the incident protons interacted inelastically. The targets were each $\frac{1}{4}$ in. in diameter and were 3.14 in., 2.23 in., and 0.85 in. long, respectively.

In order to position the proton beam properly on a target, we observed the ratio of the 90° monitor rate to the SEM as a function of the vertical and horizontal positions of the beam. Figure 1 shows the results of a typical horizontal target sweep with a $\frac{1}{4}$-in.-diam target. The flat peak of the curve demonstrates that the beam size is smaller than the target diameter.

B. Spectrometer

Figure 2 shows a schematic view of the magnetic spectrometer used to observe the particle production at 77 mrad to the incident beam line. The spectrometer, of 330 ft. length, consisted of a quadrupole doublet, two collimators, two dipoles, and four scintillation hodoscopes H_1–H_4. The magnets were all main ring components of the Fermilab accelerator. The magnetic analysis

was made by a 16-mrad deflection in each of the 20-ft-long dipoles. At maximum field the spectrometer could analyze 200-GeV/c particles. The focusing system imaged the target onto the final hodoscope with a horizontal magnification of ~2 and a vertical magnification of ~20. The horizontal angular aperture was ~±1.5 mrad and the vertical, ±3.0 mrad. The solid angle subtended by the spectrometer was ~20 μsr and momentum acceptance was ~±4%. Figure 3 shows the solid angle of the spectrometer as a function of $\Delta p/p_0$, where p_0 is the central momentum. The integrated product of the solid angle and momentum acceptance was 1.7×10^{-6} sr.

Each of the first three hodoscopes consisted of a 4-in.-wide, 2-in.-high, $\frac{1}{4}$-in.-thick trigger counter (A), followed by an array of five horizontal and 17 vertical $\frac{1}{8}$-in.-thick scintillator channels. The vertical channels were 0.22-in.-wide and the horizontal channels were 0.35-in.-wide. The final hodoscope (H_4) was larger and consisted of a 6-in.-wide, 3-in.-high, $\frac{1}{4}$-in.-thick trigger counter (A_4), followed by an array of 17 0.35-in.-wide vertical elements and five 0.6-in.-wide horizontal elements.

The arrangement of hodoscopes allowed us to determine the momentum of individual events with a precision of ±1% and to reconstruct the position of the track at the target to within ±0.4 in. horizontally and ±0.08 in. vertically. The constraint that events come from the target was essential to eliminate background at high transverse momentum.

Particles were identified by two Čerenkov counters located upstream and downstream of the second bending magnet. Each Čerenkov counter consisted of an 80-ft.-long, 1-ft.-diam stainless steel tube with nonreflecting walls. The tube was bolted to a 6-ft.-long optics section. The Čerenkov light was split into two angular channels (0–9 and 9–38
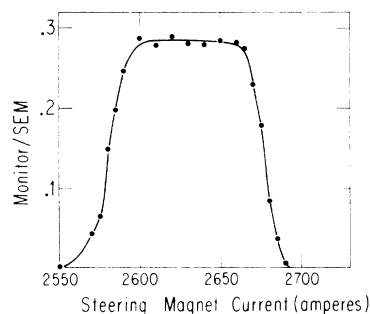

FIG. 1. Plot of the ratio of the 90° monitor rate to SEM as a function of horizontal beam position on the target. The beam position is measured in terms of current in a horizontal steering magnet.
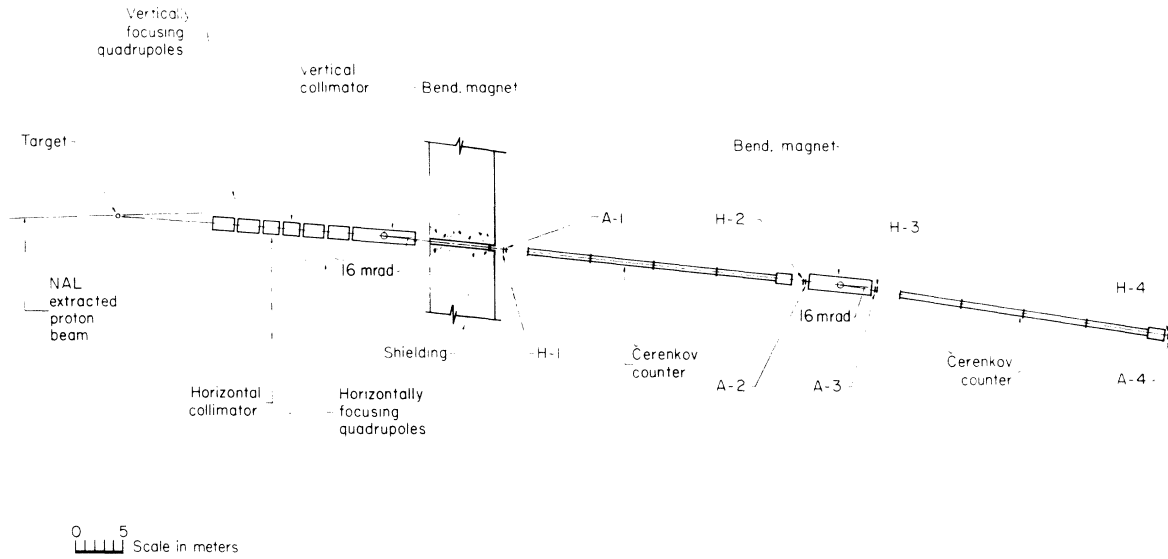
FIG. 2. Schematic view of the experimental arrangement. The particle identification system placed behind H_4 (see text) is not shown.

mrad), and focused on a 2-in. photomultiplier (RCA 31000M) in each channel.

The photomultipliers had high quantum efficiency and could resolve individual photoelectrons. With a threshold requirement of ≥ 2 photoelectrons, the counter was >99% efficient when the Čerenkov angle exceeded 3.5 mrad. Both He and CO_2 were used as gas fillings at pressures ranging from ~0 to 10 atm.

The gas pressure was measured with a precision transducer to ±0.1%. The temperature was measured at five locations along the counter with a precision of ±0.5 °C. The counter walls were in thermal contact with a water jacket in which the water was continuously circulated. In addition, the counter was surrounded with thermal insulation. With these precautions the temperature of the gas was uniform within the measurement accuracy over the length of the counter.

A particle identification system was placed behind hodoscope H_4; it consisted of an electron shower counter, a hadron calorimeter, and a muon filter. This part of the apparatus (not shown in Fig. 2) was essential in studies of the production of direct muons and the production of heavy weakly interacting particles. In the experiment described here, we only used the muon identifier to check calculated decay corrections for π and K mesons.

The apparatus was normally triggered by a triple coincidence $A_2A_3A_4$. The counter A_1 was not used in the coincidence because of its very high singles rate. When the system was triggered, the pulse heights of all four A counters, the Čerenkov coun-

ters, and the counters in the particle identifier were recorded. The status of all the hodoscope counters was encoded. All the data were accumulated in a PDP 9 computer and recorded on magnetic tape. Various on-line display programs were employed to monitor the operation of the apparatus. Other external data such as magnet currents, Čerenkov temperature, and pressure were continuously monitored and recorded by the computer. In addition, parallel scalar readouts were made of appropriate counter combinations so that preliminary cross sections and particle ratios could be calculated with a slide rule.

In anticipation of very large rates at low momentum, we could remotely replace the hodoscopes with a set of smaller trigger counters. Counters of 1-in.-high by 1-in.-wide by $\frac{1}{8}$-in.-thick (α) or $\frac{1}{4}$-in.-high by $\frac{1}{4}$-in.-wide by $\frac{1}{8}$-in.-thick (β) were
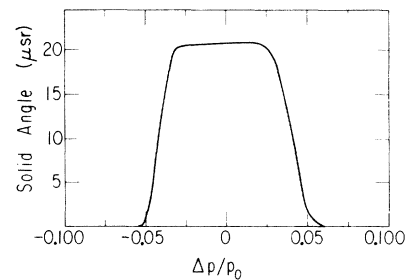

FIG. 3. Solid angle of the spectrometer as a function of $\Delta p/p_0$, where p_0 is the central momentum and Δp is the deviation in momentum from the central momentum.

available. These counters were used extensively at low momentum in early runs. In later runs they were unnecessary because the beam intensity was adjustable over a very broad range with the beam splitter.

III. DATA ACQUISITION

The measurements taken were of two basic types: (1) a measurement of $\pi^\pm$, $K^\pm$, p, and $\bar{p}$ production with the $\frac{1}{8}$-in.-diam by 2-in.-long W target at 200, 300, and 400 GeV, and (2) a comparison of yields from the $\frac{1}{4}$-in.-diam targets of Be, Ti, and W of lengths corresponding to 0.2 inelastic nuclear interaction lengths.[9] The latter measurements were important in deriving equivalent proton-nucleon cross sections. Before any extended run began, we carefully positioned the incident proton beam on the target. The position of the target stage when a given target was set on the axis of the spectrometer was determined before each running period by optical survey. The correct position of the beam on the target was verified by sweeping the beam across the target as previously discussed. The ratio of the 90° monitor rate of the SEM was sensitive to the beam position and was continuously monitored.

In the earliest runs the beam intensity could not be easily varied. Consequently, below 40 GeV/c ($p_\perp = 3.05$ GeV/c) we used the smaller counters instead of the hodoscopes to reduce the counting rates. Runs of both types were made at 40 GeV/c to provide overlap of the data. These runs were made with 300-GeV and 200-GeV protons incident on a 2-in.-long by $\frac{1}{8}$-in.-diam W target. Results from these runs have already been published.[10]

The run with 400 GeV/c was carried out later with the same W target. A brief run with 300-GeV incident protons was made immediately after the 400-GeV run to ensure a direct comparison between the two energies. Finally, runs were made with 300-GeV protons incident on the Be, Ti, and W targets of identical interaction length. Also, measurements of d and $\bar{d}$ production, as well as searches for direct muon production and massive weakly interacting particles, were carried out. The results of the latter two investigations are reported elsewhere.[11, 12]

During the course of measurements the quality and intensity of the Fermilab beam steadily improved. The beam intensity that could be used was limited by the rate of accidental extra hits in the front hodoscope H_1. Such events gave an ambiguity in the reconstruction of the origin of the event at the target. In the early runs we were limited to an intensity $\leqslant 10^{11}$ protons/pulse. As the quality of

the spill improved, we were able to use as much as 5×10^{11} protons/pulse with an accidental rate $\lesssim 10\%$ in H_1. The accidental rate in A_1, which was at the same location, served as a monitor to the accidental rate in H_1 and was continuously recorded. Also, the introduction of beam-splitting permitted measurements over the entire range of spectrometer momenta with the hodoscope system. Throughout the experiment we had many opportunities to repeat measurements with 300-GeV incident protons. The quality of agreement of these results ($\pm 5\%$) gave a measure of the systematic errors in the experiment.

The particle ratios were determined by appropriate adjustment of the pressure in the Čerenkov counters at each spectrometer momentum setting. Figure 4 shows a pressure curve taken at 39 GeV/c to evaluate the performance of the counter. During most of the data-taking the two Čerenkov counters were set such that the upstream counter counted pions in the large-angle channel and kaons in the small-angle channel, while the downstream counter was set to count pions only. Events for which neither of the two Čerenkov counters counted were considered protons. The efficiency of the counter, plotted in Fig. 4, was found to be greater than 99.95% when the CO_2 pressure exceeded 1 atm. In the early runs only one Čerenkov counter was available. In this circumstance two separate runs were taken to measure the fraction of π, K, and p in the beam.

A special run was taken for the detection of deuterons and antideuterons. In this run the upstream Čerenkov counter was set to veto in the trigger
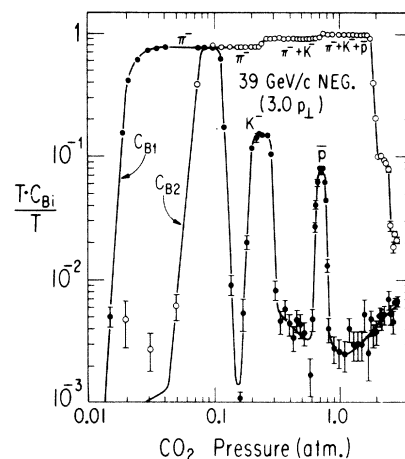

FIG. 4. Pressure curve for a 39-GeV/c negative beam for Čerenkov counter. The curve marked with closed circles is for the 0–9 mrad channel (C_{B1}). The curve marked with open circles is for the 9–38 mrad channel (C_{B2}). The ordinate is the measured Čerenkov counter efficiency.

pions, kaons, and protons (antiprotons), while the downstream counter was set at a pressure to record deuterons (antideuterons) in the outer channel. The downstream Čerenkov counter was not placed in the trigger; the pulse heights of its two channels were recorded.

The central momentum of the spectrometer was determined by the Fermilab calibration of the main ring dipoles. This calibration was verified with the Čerenkov counter. A pressure curve was taken with 45-GeV/c protons (antiprotons) in the region where the Čerenkov angle passed the 9-mrad boundary between the inner channel and the outer channel. Precise knowledge of the geometry of the optical system and the index of refraction of He, which has a very low dispersion, permits an accurate calibration of the beam momentum. Figure 5 shows the efficiency of the inner and outer Čerenkov channels in the region where the proton light moves across the 9-mrad boundary as the index of refraction is varied. In terms of the extrapolated indices of refraction shown in Fig. 5, the momentum of the protons is given by

$$p = \{m^2/[(n-1)_1 + (n-1)_2 - \theta^2]\}^{1/2} ,$$

where m is the proton mass, θ is the boundary angle between the two channels, and $(n-1)_1$ and $(n-1)_2$ are the indices of refraction extrapolated as shown in Fig. 5 for the inner and outer channels, respectively. With $\theta^2 = (81 \pm 3) \times 10^{-6}$ we find $p = 45.15 \pm 0.25$ GeV/c.

A similar calibration with the spectrometer set

for negative particles gave $p = 45.15 \pm 0.30$ GeV/c. Later calibration during the 400-GeV run with positive particles gave 45.25 ± 0.25 GeV/c.

IV. DATA REDUCTION

For each spectrometer momentum setting and polarity the cross section per nucleus for the production of all charged particles was computed. The fraction of each particle species was determined with the Čerenkov counters.

Data were treated differently above and below the spectrometer setting of 40 GeV/c. Above 40 GeV/c ($p_\perp = 3.05$ GeV/c) all the events were reconstructed with the hodoscope information. Distributions were made of the horizontal and vertical positions of all events at the target. Typical distributions are shown in Fig. 6 for a run at 40 GeV/c. At this spectrometer setting less than 2% of the events fail to come within ± 1 in. horizontally and ± 0.16 in. vertically from the nominal target position. Hence, below 40 GeV/c the yields are taken to be proportional to the counting rate/incident proton and are normalized to the yield of reconstructed events at 40 GeV/c.

For spectrometer settings above 40 GeV/c it was necessary to derive the yield from reconstructed events. At very high $p_\perp$ (≥ 6 GeV/c) the apparatus was most often triggered by a background muon passing through A_3 and A_4 coupled with a random count in A_2. Such events do not reconstruct, since the H_1 hodoscope does not register. In case H_1 does register, the reconstructed trajectories upstream and downstream of the second bending magnet may fail to intersect in the center of that magnet. In almost all cases where continuity at the second bending magnet is pre-
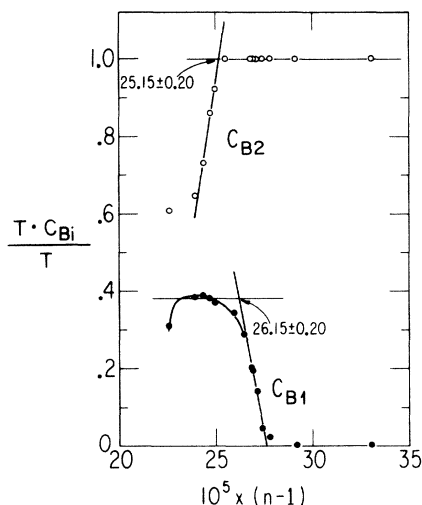

FIG. 5. Pressure curve for 45-GeV/c protons in Čerenkov counter. The pressure has been expressed in terms of the index of refraction of the helium gas. The closed circles give the efficiency for the inner channel; the open circles give the efficiency for the outer channel. The ordinate is the measured Čerenkov counter efficiency.
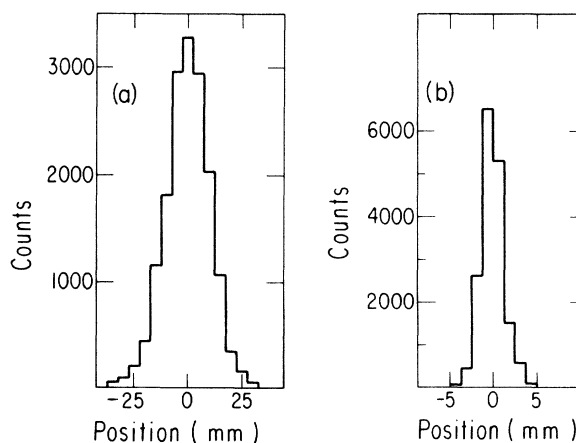

FIG. 6. Horizontal (a) and vertical (b) reconstructed target position distributions for 40-GeV/c particles.

served, we find that the track indeed comes from the target.

The yield of reconstructed events was slightly rate-dependent owing to accidental extra counts in H_1. Hodoscope H_1 and its associated counter A_1 where the only rate-dependent elements in the entire spectrometer. The accidental rate in H_1 was proportional to the accidental rate in the scintillator A_1, which was continuously monitored. The intensity of the incident proton beam was adjusted to keep the loss correction less than 10%. The only exceptions were runs at high transverse momentum where 20% losses were tolerated in order to increase the rate of data acquisition.

Most of the data below 40 GeV/c ($p_\perp = 3.05$ GeV/c) were taken with an arrangement of smaller trigger counters, either $\alpha_1\alpha_2\alpha_3 A_4$ or $\beta_1\alpha_2\alpha_3 A_4$. In each case the solid angle was smaller, and the momentum "bite" was $\pm 3\%$. The yields measured in these runs were normalized at 40 GeV/c to the yields measured at the same momentum with the hodoscopes.

In the later runs, when the beam-splitting became available, data were taken with the normal arrangement at momenta below 40 GeV/c. These data were in excellent agreement with data taken earlier with the small counter arrangement.

All yields were first normalized to the 90° monitor. In turn, the 90° monitor calibration, with respect to the SEM, was established by averaging over all the runs. In this average some runs were eliminated where the SEM was malfunctioning or the targeting efficiency was poor. Using the SEM radiochemical calibration, we obtained the total particle yield per incident proton.

The particle ratios observed at the end of the detector were obtained from the Čerenkov data in a straightforward manner. The yields of K mesons and pions required correction for decay. For pions the correction factor ranged from 1.16 at 10 GeV/c ($p_\perp = 0.75$ GeV/c) to 1.01 at 100 GeV/c. For kaons the correction was larger, ranging from a factor 3.6 at 10 GeV/c to a factor 1.11 at 100 GeV/c.

With the above information the yield Y_i per incident proton for each particle species was computed. In addition to the decay corrections, two further corrections were made to the yield Y_i which were, to a good approximation, common to all particle species (except deuterons and anti-deuterons). Nuclear absorption due to material in the spectrometer required a correction of 1.15. In some cases the gas pressure in the Čerenkov counters was significant and a correction as large as 1.25 was required for nuclear absorption in the spectrometer. The nuclear absorption was computed on the basis of inelastic nuclear cross sections.[9] Below 40 GeV/c multiple scattering cor-

rections were necessary. These ranged from 1.33 at 10 GeV/c to no correction at 40 GeV/c and above.

Calculation of the solid angle, momentum "bite," decay correction, and multiple scattering correction were all made with a Monte Carlo program which traced in detail charged particles through the spectrometer.

We have calculated the invariant cross section per nucleus for the production of particle species i using the following formula:

$$\frac{E d\sigma_A^i}{d^3 p} = \frac{A}{\rho L N_0} \; \frac{Y_i}{p^2 \Delta\Omega \, \Delta p/p} \; \exp\left(\frac{N_0 \rho L \sigma_{\text{abs}}}{A}\right) \, ,$$

where A, ρ, σ_{abs}, and L are the atomic number, density, absorption cross section, and length, respectively, of the target; N_0 is Avogadro's number, Y_i is the corrected yield per incident proton of the particle species i, $\Delta\Omega \, \Delta p/p = 1.7 \times 10^{-6}$ sr is the spectrometer acceptance, and p is the secondary momentum in the laboratory. The exponential factor in the formula accounts for the absorption in the target itself of both the incoming proton and the outgoing particle.

We calculated the absolute cross sections, using data from runs at 300 GeV/c with the three nuclear targets of 0.2 interaction lengths. These data were used because the $\frac{1}{4}$-in.-diam targets intercepted all the incident proton beam. The relative yields at the three energies with the $\frac{1}{8}$-in.-diam, 2-in.-long W target were well determined, and the absolute cross sections were obtained by normalization to the yield with the $\frac{1}{4}$-in.-diam W target at 40-GeV/c spectrometer momentum and 300-GeV incident proton energy.

A few runs were made at 40-GeV/c spectrometer momentum and 300-GeV incident proton energy to compare the yields from $\frac{1}{4}$-in.-diam W targets of lengths of 0.85 in. and 2.0 in., corresponding to 0.2 and 0.4 interaction lengths, respectively. The cross sections which we obtained for the production of pions agreed within 10%, indicating that the thick target absorption correction used in the cross-section formula was reasonable.

The statistical errors were less than 5% for measurements at 80 GeV/c ($p_\perp = 6.10$ GeV/c) and below. A 5% systematic error was assigned to the measurements at 80 GeV/c and below. This error was based on reproducibility of the measurements. Extensive repetition of measurements was carried out with the spectrometer set at 40 GeV/c to establish the degree of reproducibility. Above 80 GeV/c statistical errors dominate.

V. RESULTS

The measured invariant cross sections *per nucleus* are presented in a series of tables. The

errors quoted include all systematic and statistical errors, except the over-all $\pm 25\%$ systematic error associated with the absolute normalization of the incident proton beam flux.

In Table I we present the invariant cross section per W nucleus for production of π^+ and π^- as a function of $p_\perp$ for incident proton energies of 200, 300, and 400 GeV. In Table II the cross-section ratios K^+/π^+ and K^-/π^- produced by 200-, 300-, and 400-GeV protons incident on a W nucleus are presented as a function of transverse momentum. In Table III the cross-section ratios p/π^+ and $\bar{p}/\pi^-$ are presented for the same conditions. In Table IV the cross-section ratios d/π^+, $\bar{d}/\pi^-$, d/p, and $\bar{d}/\bar{p}$ produced on a W nucleus by 300-GeV incident protons are presented as a function of $p_\perp$. Table

V shows the invariant cross section per nucleus for the production of π^+ and π^- as a function of $p_\perp$, by 300-GeV protons incident on targets of Be, Ti, and W. In Table VI the particle ratios K^+/π^+ and K^-/π^- produced by 300-GeV protons incident on targets of Be, Ti, and W are presented as a function of $p_\perp$. In Tables VII and VIII the particle ratios p/π^+, $\bar{p}/\pi^-$, and d/π^+, $\bar{d}/\pi^-$, respectively, are presented for the same conditions.

VI. DISCUSSION OF RESULTS

A. Pion production

In the preliminary report of this work[10] we used a very elementary method to estimate the effective number of nucleons (A_{eff}) in W. We assumed that

TABLE I. Invariant cross section per nucleus for $\pi^\pm$ mesons produced at $\sim 90°$ c.m. in p-W collisions. At each $p_\perp$ value the top line refers to π^+ and the bottom line to π^-. Errors do not include the uncertainty in the absolute calibration.

$p_\perp$ (GeV/c)	$Ed\sigma(\pi^\pm)/d^3p$ (cm^{2}GeV^{-2})		
	200 GeV	300 GeV	400 GeV
0.76	$(1.22 \pm 0.12) \times 10^{-25}$	$(1.36 \pm 0.14) \times 10^{-25}$	$(1.61 \pm 0.16) \times 10^{-25}$
	$(1.13 \pm 0.11) \times 10^{-25}$	$(1.39 \pm 0.14) \times 10^{-25}$	$(1.50 \pm 0.15) \times 10^{-25}$
1.14	$(2.34 \pm 0.12) \times 10^{-26}$	$(2.44 \pm 0.12) \times 10^{-26}$	$(2.48 \pm 0.12) \times 10^{-26}$
	$(1.74 \pm 0.09) \times 10^{-26}$	$(2.24 \pm 0.11) \times 10^{-26}$	$(2.16 \pm 0.11) \times 10^{-26}$
1.53	$(3.81 \pm 0.19) \times 10^{-27}$	$(3.96 \pm 0.20) \times 10^{-27}$	$(4.21 \pm 0.21) \times 10^{-27}$
	$(2.83 \pm 0.14) \times 10^{-27}$	$(3.77 \pm 0.19) \times 10^{-27}$	$(3.87 \pm 0.19) \times 10^{-27}$
2.29	$(1.73 \pm 0.09) \times 10^{-28}$	$(2.00 \pm 0.10) \times 10^{-28}$	$(2.21 \pm 0.11) \times 10^{-28}$
	$(1.25 \pm 0.06) \times 10^{-28}$	$(1.83 \pm 0.09) \times 10^{-28}$	$(1.99 \pm 0.10) \times 10^{-28}$
3.05	$(8.35 \pm 0.42) \times 10^{-30}$	$(1.18 \pm 0.06) \times 10^{-29}$	$(1.50 \pm 0.07) \times 10^{-29}$
	$(6.55 \pm 0.33) \times 10^{-30}$	$(1.06 \pm 0.05) \times 10^{-29}$	$(1.33 \pm 0.07) \times 10^{-29}$
3.82	$(4.54 \pm 0.23) \times 10^{-31}$	$(8.63 \pm 0.43) \times 10^{-31}$	$(1.13 \pm 0.06) \times 10^{-30}$
	$(3.35 \pm 0.17) \times 10^{-31}$	$(7.73 \pm 0.39) \times 10^{-31}$	$(0.98 \pm 0.05) \times 10^{-30}$
4.58	$(2.58 \pm 0.13) \times 10^{-32}$	$(6.29 \pm 0.31) \times 10^{-32}$	$(1.05 \pm 0.05) \times 10^{-31}$
	$(1.91 \pm 0.10) \times 10^{-32}$	$(5.97 \pm 0.30) \times 10^{-32}$	$(0.86 \pm 0.04) \times 10^{-31}$
5.34	$(1.59 \pm 0.08) \times 10^{-33}$	$(6.46 \pm 0.32) \times 10^{-33}$	$(1.04 \pm 0.05) \times 10^{-32}$
	$(1.11 \pm 0.06) \times 10^{-33}$	$(5.27 \pm 0.26) \times 10^{-33}$	$(0.86 \pm 0.04) \times 10^{-32}$
6.10	$(8.7 \pm 1.2) \times 10^{-35}$	$(6.43 \pm 0.32) \times 10^{-34}$	$(1.39 \pm 0.07) \times 10^{-33}$
	$(7.07 \pm 0.82) \times 10^{-35}$	$(5.12 \pm 0.26) \times 10^{-34}$	$(1.16 \pm 0.06) \times 10^{-33}$
6.87	$(4.5 \pm 1.1) \times 10^{-36}$	$\cdots$	$(1.78 \pm 0.11) \times 10^{-34}$
	$(3.5 \pm 1.0) \times 10^{-36}$	$(5.12 \pm 0.69) \times 10^{-35}$	$(1.58 \pm 0.09) \times 10^{-34}$
7.25	$\cdots$		
	$(1.1 \pm 0.6) \times 10^{-36}$		
7.63		$(4.6 \pm 1.3) \times 10^{-36}$	$(2.39 \pm 0.40) \times 10^{-35}$
		$(5.5 \pm 1.3) \times 10^{-36}$	$(2.31 \pm 0.34) \times 10^{-35}$
8.39		$\cdots$	$(2.5 \pm 0.7) \times 10^{-36}$
		$(4.4 \pm 2.6) \times 10^{-37}$	$(3.2 \pm 1.1) \times 10^{-36}$
9.16		$\cdots$	
		$< 8.9 \times 10^{-38}$ [a]	

[a] 90% confidence limit.

TABLE II. K^+/π^+ (top line) and K^-/π^- (bottom line) cross-section ratios for W target.

$p_\perp$ (GeV/c)	Particle ratio $K^\pm/\pi^\pm$		
	200 GeV	300 GeV	400 GeV
0.76	0.24 ± 0.04	0.21 ± 0.02	0.23 ± 0.03
	0.15 ± 0.03	0.14 ± 0.02	0.15 ± 0.04
1.14	0.32 ± 0.03	0.31 ± 0.02	0.31 ± 0.03
	0.20 ± 0.02	0.20 ± 0.02	0.22 ± 0.02
1.53	0.39 ± 0.03	0.360 ± 0.016	0.395 ± 0.028
	0.200 ± 0.014	0.202 ± 0.008	0.225 ± 0.016
2.29	0.445 ± 0.024	0.433 ± 0.018	0.439 ± 0.028
	0.207 ± 0.010	0.242 ± 0.010	0.282 ± 0.019
3.05	0.485 ± 0.015	0.506 ± 0.019	0.500 ± 0.026
	0.201 ± 0.006	0.248 ± 0.010	0.274 ± 0.011
3.82	0.522 ± 0.024	0.543 ± 0.020	0.543 ± 0.029
	0.191 ± 0.007	0.230 ± 0.009	0.248 ± 0.008
4.58	0.536 ± 0.033	0.535 ± 0.022	0.490 ± 0.030
	0.170 ± 0.014	0.198 ± 0.008	0.222 ± 0.009
.5.34	0.64 ± 0.07	0.531 ± 0.035	0.712 ± 0.044
	0.15 ± 0.03	0.167 ± 0.008	0.188 ± 0.010
6.10	0.55 ± 0.19	0.53 ± 0.05	0.66 ± 0.06
	0.08 ± 0.07	0.115 ± 0.011	0.112 ± 0.022
6.87		$\cdots$	0.71 ± 0.15
		0.10 ± 0.03	0.060 ± 0.023
7.63		$\cdots$	
		0.05 ± 0.05	

TABLE III. p/π^+ (top line) and $\bar{p}/\pi^-$ (bottom line) cross-section ratios for W target.

$p_\perp$ (GeV/c)	Particle ratio p/π		
	200 GeV	300 GeV	400 GeV
0.76	0.43 ± 0.02	0.34 ± 0.02	0.35 ± 0.02
	0.105 ± 0.030	0.08 ± 0.01	0.07 ± 0.01
1.14	0.632 ± 0.006	0.531 ± 0.020	0.530 ± 0.010
	0.107 ± 0.005	0.105 ± 0.005	0.127 ± 0.002
1.53	0.834 ± 0.009	0.669 ± 0.020	0.685 ± 0.010
	0.109 ± 0.002	0.126 ± 0.004	0.146 ± 0.003
2.29	1.033 ± 0.012	0.872 ± 0.020	0.811 ± 0.015
	0.095 ± 0.003	0.115 ± 0.002	0.139 ± 0.004
3.05	1.093 ± 0.011	0.865 ± 0.008	0.788 ± 0.016
	0.076 ± 0.001	0.089 ± 0.002	0.102 ± 0.003
3.82	1.07 ± 0.02	0.827 ± 0.020	0.689 ± 0.018
	0.044 ± 0.003	0.061 ± 0.002	0.076 ± 0.003
4.58	1.11 ± 0.03	0.736 ± 0.020	0.616 ± 0.018
	0.033 ± 0.003	0.041 ± 0.002	0.047 ± 0.003
5.34	1.09 ± 0.07	0.60 ± 0.02	0.553 ± 0.024
	0.029 ± 0.014	0.023 ± 0.002	0.032 ± 0.004
6.10	0.98 ± 0.17	0.56 ± 0.04	0.38 ± 0.03
	< 0.01	0.013 ± 0.003	0.011 ± 0.005
6.87		$\cdots$	0.36 ± 0.08
		0.01 ± 0.01	0.006 ± 0.006

A_{eff} for W was given by $\sigma_{\text{abs}}/\sigma_p = \frac{1635}{40} = 40.9$, where σ_{abs} is the absorption cross section in W (1635 mb)[9] and σ_p is the p-p total cross section (40 mb). Subsequent work with targets of different A has shown that this method of reduction of the cross section per nucleus to cross section per nucleon is too naive. Nevertheless, we will discuss some of the features of the data with this reduction scheme before using a more sophisticated method (see part E below). Certain dominant features of the data do not depend on the reduction scheme and are thus features which are least sensitive to the method of derivation of the cross section.

Figures 7 and 8 show the invariant cross sections per "nucleon" (cross section per nucleus divided by 40.9) for π^+ and π^- production, respectively, for 200-, 300-, and 400-GeV incident protons. Smooth curves drawn through the data points in these figures and subsequent figures are only intended to guide the eye. For all energies and at large $p_\perp$ the cross sections fall exponentially; they do not show a manifest power-law dependence. The energy dependence, very small at low $p_\perp$, grows stronger as $p_\perp$ increases. This is in agreement with other experiments at the CERN ISR[3-5] and at Fermilab.[13, 14]

Most of the theoretical models which have been proposed predict for the single-pion inclusive cross section at $\sim 90°$ c.m. a behavior at high $p_\perp$, of the form $(\sqrt{s})^{-n} f(x_\perp)$, where s is the square of the c.m. energy of the collision and $f(x_\perp)$ is a function of the scaling variable $x_\perp = 2p_\perp/\sqrt{s}$. If our pion data can indeed be expressed in such a form, then the logarithm of the cross section plotted

TABLE IV. d/π^+, d/p (top line) and $\bar{d}/\pi^-$, $\bar{d}/\bar{p}$ (bottom line) cross-section ratios for W target.

$p_\perp$ (GeV/c)	300 GeV	
	d/π	d/p
2.29	$(47 \pm 5) \times 10^{-4}$	$(5.4 \pm 0.6) \times 10^{-3}$
	$(1.42 \pm 0.14) \times 10^{-4}$	$(1.23 \pm 0.12) \times 10^{-3}$
3.05	$(66 \pm 6) \times 10^{-4}$	$(7.6 \pm 0.8) \times 10^{-3}$
	$(1.0 \pm 0.1) \times 10^{-4}$	$(1.12 \pm 0.11) \times 10^{-3}$
3.82	$(52 \pm 5) \times 10^{-4}$	$(6.3 \pm 0.6) \times 10^{-3}$
	$(0.91 \pm 0.15) \times 10^{-4}$	$(1.49 \pm 0.25) \times 10^{-3}$
4.58	$(45 \pm 5) \times 10^{-4}$	$(6.1 \pm 0.6) \times 10^{-3}$
	$(0.22 \pm 0.13) \times 10^{-4}$	$(0.54 \pm 0.32 \times 10^{-3}$
5.34	$(26 \pm 11) \times 10^{-4}$	$(4.3 \pm 1.8) \times 10^{-3}$
	$\cdots$	$\cdots$

TABLE V. Invariant cross section per nucleus for $\pi^{\pm}$ mesons produced at 90° c.m. in p-Be, p-Ti, and p-W collisions for 300-GeV incident protons. At each $p_{\perp}$ value the top line refers to π^{+} and the bottom line to π^{-}.

$p_{\perp}$ (GeV/c)	$E d\sigma(\pi^{\pm})/d^3p$ (cm^2 GeV^{-2})		
	Be	Ti	W
0.76	$(1.11 \pm 0.10) \times 10^{-26}$	$(4.80 \pm 0.48) \times 10^{-26}$	$(1.36 \pm 0.14) \times 10^{-25}$
	$(1.10 \pm 0.10) \times 10^{-26}$	$(4.71 \pm 0.47) \times 10^{-26}$	$(1.39 \pm 0.14) \times 10^{-25}$
1.14	$(1.75 \pm 0.09) \times 10^{-27}$	$(7.93 \pm 0.40) \times 10^{-27}$	$(2.44 \pm 0.12) \times 10^{-26}$
	$(1.48 \pm 0.08) \times 10^{-27}$	$(6.98 \pm 0.35) \times 10^{-27}$	$(2.24 \pm 0.11) \times 10^{-26}$
1.53	$(2.43 \pm 0.12) \times 10^{-28}$	$(1.22 \pm 0.06) \times 10^{-27}$	$(3.96 \pm 0.20) \times 10^{-27}$
	$(2.20 \pm 0.11) \times 10^{-28}$	$(1.14 \pm 0.06) \times 10^{-27}$	$(3.77 \pm 0.19) \times 10^{-27}$
2.29	$(1.02 \pm 0.05) \times 10^{-29}$	$(5.62 \pm 0.28) \times 10^{-29}$	$(2.00 \pm 0.10) \times 10^{-28}$
	$(0.85 \pm 0.04) \times 10^{-29}$	$(4.92 \pm 0.25) \times 10^{-29}$	$(1.83 \pm 0.09) \times 10^{-28}$
3.05	$(4.70 \pm 0.24) \times 10^{-31}$	$(2.95 \pm 0.15) \times 10^{-30}$	$(1.18 \pm 0.06) \times 10^{-29}$
	$(4.10 \pm 0.21) \times 10^{-31}$	$(2.50 \pm 0.13) \times 10^{-30}$	$(1.06 \pm 0.05) \times 10^{-29}$
3.82	$(3.25 \pm 0.16) \times 10^{-32}$	$(2.12 \pm 0.11) \times 10^{-31}$	$(8.63 \pm 0.43) \times 10^{-31}$
	$(2.70 \pm 0.14) \times 10^{-32}$	$(1.84 \pm 0.09) \times 10^{-31}$	$(7.73 \pm 0.39) \times 10^{-31}$
4.58	$(2.11 \pm 0.11) \times 10^{-33}$	$(1.51 \pm 0.08) \times 10^{-32}$	$(6.29 \pm 0.31) \times 10^{-32}$
	$(2.03 \pm 0.10) \times 10^{-33}$	$(1.37 \pm 0.07) \times 10^{-32}$	$(5.97 \pm 0.30) \times 10^{-32}$
5.34	$(2.11 \pm 0.11) \times 10^{-34}$	$(1.36 \pm 0.07) \times 10^{-33}$	$(6.46 \pm 0.32) \times 10^{-33}$
	$(1.67 \pm 0.09) \times 10^{-34}$	$(1.12 \pm 0.06) \times 10^{-33}$	$(5.27 \pm 0.26) \times 10^{-33}$
6.10	$(2.62 \pm 0.18) \times 10^{-35}$	$(1.60 \pm 0.10) \times 10^{-34}$	$(6.43 \pm 0.32) \times 10^{-34}$
	$(1.59 \pm 0.10) \times 10^{-35}$	$(1.02 \pm 0.08) \times 10^{-34}$	$(5.12 \pm 0.26) \times 10^{-34}$

TABLE VI. K^{+}/π^{+} (top line) and K^{-}/π^{-} (bottom line) cross-section ratios for 300-GeV protons incident on Be, Ti, and W targets.

$p_{\perp}$ (GeV/c)	Particle ratio K/π		
	Be	Ti	W
0.76	0.17 ± 0.02	0.21 ± 0.02	0.21 ± 0.02
	0.12 ± 0.01	0.14 ± 0.02	0.14 ± 0.02
1.14	0.27 ± 0.02	0.29 ± 0.02	0.31 ± 0.02
	0.17 ± 0.01	0.18 ± 0.02	0.20 ± 0.02
1.53	0.310 ± 0.017	0.353 ± 0.019	0.360 ± 0.016
	0.192 ± 0.012	0.205 ± 0.013	0.202 ± 0.008
2.29	0.400 ± 0.021	0.426 ± 0.023	0.433 ± 0.018
	0.232 ± 0.013	0.236 ± 0.013	0.242 ± 0.010
3.05	0.447 ± 0.024	0.459 ± 0.026	0.506 ± 0.019
	0.238 ± 0.014	0.234 ± 0.012	0.248 ± 0.010
3.82	0.457 ± 0.026	0.479 ± 0.027	0.543 ± 0.020
	0.189 ± 0.011	0.211 ± 0.012	0.230 ± 0.009
4.58	0.510 ± 0.029	0.521 ± 0.030	0.535 ± 0.022
	0.162 ± 0.010	0.195 ± 0.012	0.198 ± 0.008
5.34	0.470 ± 0.027	0.517 ± 0.030	0.531 ± 0.035
	0.106 ± 0.008	0.154 ± 0.011	0.167 ± 0.008
6.10	0.377 ± 0.042	0.539 ± 0.049	0.53 ± 0.05
	0.079 ± 0.016	0.102 ± 0.013	0.115 ± 0.011

TABLE VII. p/π^{+} (top line) and $\bar{p}/\pi^{-}$ (bottom line) cross-section ratios for 300-GeV protons incident on Be, Ti, and W targets.

$p_{\perp}$ (GeV/c)	Particle ratio p/π		
	Be	Ti	W
0.76	0.26 ± 0.01	0.31 ± 0.01	0.34 ± 0.02
	0.066 ± 0.003	0.078 ± 0.004	0.077 ± 0.004
1.14	0.42 ± 0.01	0.48 ± 0.01	0.531 ± 0.020
	0.100 ± 0.003	0.105 ± 0.003	0.105 ± 0.005
1.53	0.552 ± 0.007	0.636 ± 0.008	0.669 ± 0.020
	0.114 ± 0.004	0.110 ± 0.004	0.126 ± 0.004
2.29	0.622 ± 0.008	0.767 ± 0.010	0.872 ± 0.020
	0.101 ± 0.004	0.115 ± 0.003	0.115 ± 0.002
3.05	0.610 ± 0.010	0.788 ± 0.013	0.865 ± 0.008
	0.073 ± 0.003	0.086 ± 0.002	0.089 ± 0.002
3.82	0.494 ± 0.012	0.674 ± 0.014	0.827 ± 0.020
	0.048 ± 0.003	0.065 ± 0.002	0.061 ± 0.002
4.58	0.424 ± 0.012	0.593 ± 0.015	0.736 ± 0.020
	0.025 ± 0.002	0.040 ± 0.003	0.041 ± 0.002
5.34	0.330 ± 0.011	0.484 ± 0.014	0.600 ± 0.020
	0.012 ± 0.002	0.024 ± 0.003	0.023 ± 0.002
6.10	0.263 ± 0.030	0.362 ± 0.032	0.560 ± 0.040
	0.014 ± 0.007	0.015 ± 0.004	0.013 ± 0.003

TABLE VIII. d/p (top line) and $\bar{d}/\bar{p}$ (bottom line) cross-section ratios for 300-GeV protons incident on Be, Ti, and W targets.

$p_\perp$ (GeV/c)	d/p		
	Be	Ti	W
2.29	$(3.2 \pm 0.6) \times 10^{-3}$	$(5.1 \pm 1.0) \times 10^{-3}$	$(5.4 \pm 0.6) \times 10^{-3}$
	$(1.4 \pm 0.3) \times 10^{-3}$	$(1.6 \pm 0.3) \times 10^{-3}$	$(1.2 \pm 0.1) \times 10^{-3}$
3.05	$(3.8 \pm 0.6) \times 10^{-3}$	$(5.4 \pm 1.0) \times 10^{-3}$	$(7.6 \pm 0.8) \times 10^{-3}$
3.81	$(3.8 \pm 0.8) \times 10^{-3}$	$(5.9 \pm 1.0) \times 10^{-3}$	$(6.3 \pm 0.6) \times 10^{-3}$
4.58	$(5.4 \pm 1.0) \times 10^{-3}$	$(7.2 \pm 1.0) \times 10^{-3}$	$(6.1 \pm 0.6) \times 10^{-3}$

against $x_\perp$ for all three energies should yield parallel curves, irrespective of the absolute calibration. Figure 9 shows that the curves are parallel for $x_\perp > 0.4$. A good fit to the data for $x_\perp > 0.4$ is given by the expression

$$E d\sigma/d^3 p \propto (\sqrt{s})^{-n} e^{-ax_\perp}.$$
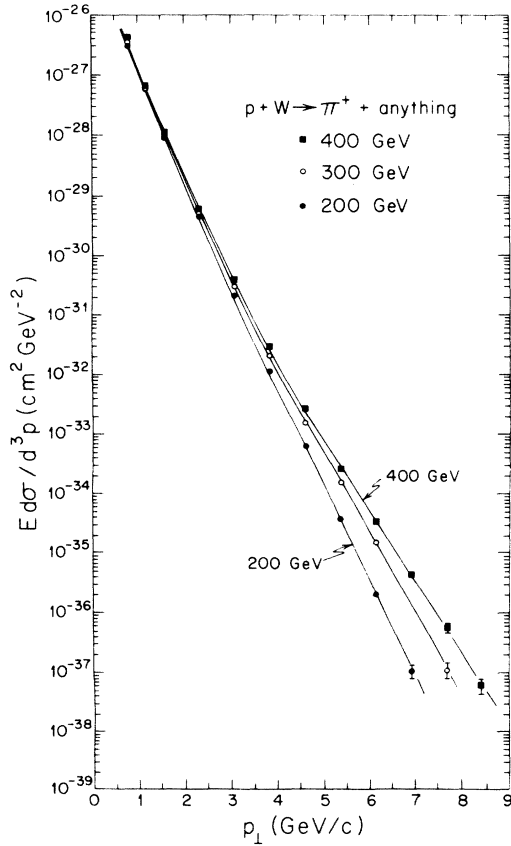
We obtain, for π^+, $n = 11.4 \pm 0.4$, $a = 36.3 \pm 0.4$; for π^-, $n = 10.8 \pm 0.4$, $a = 36.0 \pm 0.4$. Figure 10 shows this scaling for the π^- cross sections.

In a collision with a free nucleon the fixed lab angle of 77 mrad corresponds to a c.m. angle for a relativistic particle of 77°, 88°, and 97° for an incident proton of 200, 300, and 400 GeV, respectively. The Fermi motion of the nucleons in the nucleus smears the production angle in the c.m. by $\sim \pm 6°$ and the c.m. energy $(\sqrt{s})$ by $\sim \pm 10\%$. The kinematic effects of the Fermi motion appear to be small, given the observed energy dependence of the data. As we shall discuss below, the dependence of the cross section on atomic number is sufficiently strong that detailed consideration of Fermi motion is not warranted.

B. Kaon production

The cross-section ratios of K^+/π^+ and K^-/π^- from the W target are plotted in Fig. 11 as a function of $p_\perp$ for the three incident proton energies. The

FIG. 7. Invariant cross section per W nucleus *divided by 40.9* (see text) for π^+ mesons produced at 90° c.m. in p-W collisions.

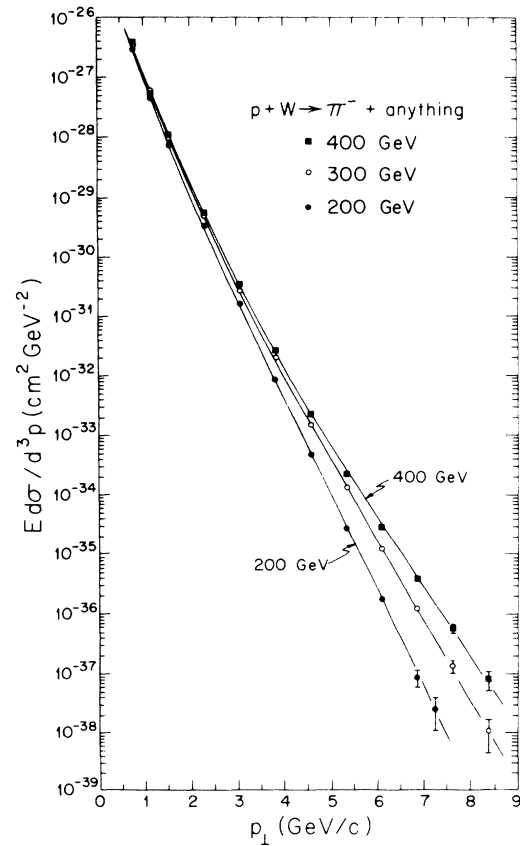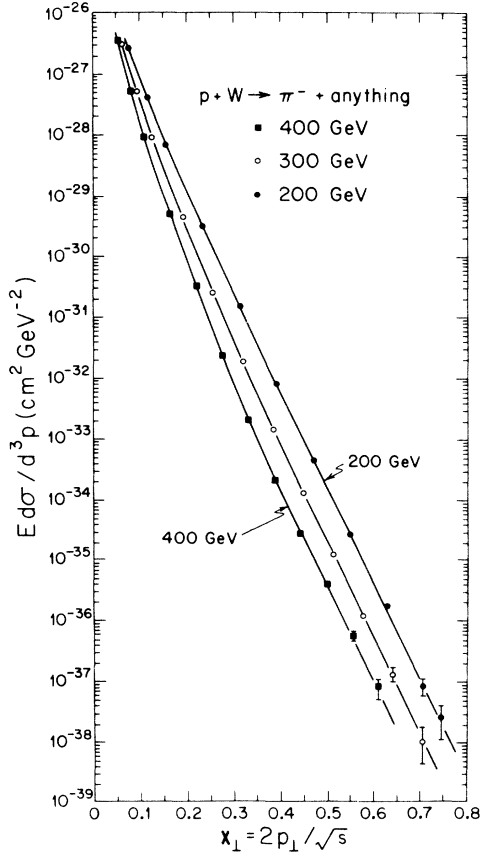
FIG. 8. Invariant cross section per W nucleus *divided by 40.9* (see text) for π^- mesons produced at 90° c.m. in p-W collisions.

FIG. 9. π^- production cross section of Fig. 8 plotted against $x_\perp$.

FIG. 10. Plot of the function $(\sqrt{s})^{10.8} E d\sigma(\pi^-)/d^3 p$ versus $x_\perp$.

ratio K^+/π^+ is essentially independent of s, rising from 0.2 at $p_\perp = 0.76$ GeV/c to ~0.55 at 4 GeV/c and beyond. The K^-/π^- ratio, while independent of s within errors at very low $p_\perp$ (< 1 GeV/c), does show a definite energy dependence at $p_\perp > 2$ GeV/c. In fact, in this region it is rather well represented by an expression of the form $\sqrt{s}\, F(p_\perp)$, where $F(p_\perp)$ is a slowly varying function with a broad maximum at $p_\perp \approx 2.5$ GeV/c and dropping by a factor of ~2 at $p_\perp \approx 6$ GeV/c. It may be appropriate here to note that the $\bar{p}/\pi^-$ ratio has a similar behavior, in particular a $\sqrt{s}$ dependence [$F(p_\perp)$, however, drops off faster].

If the $K^\pm/\pi^\pm$ ratios are plotted against the scaling variable $x_\perp = 2p_\perp/\sqrt{s}$, as in Fig. 12, one sees from the K^+/π^+ behavior that the K^+ cross section scales in the same way as the pions. At $x_\perp > 0.40$ a fit of the K^+ cross sections to $(\sqrt{s})^{-n} e^{-ax_\perp}$ yields

$$n = 10.6 \pm 0.8 \quad \text{and} \quad a = 35.0 \pm 1.5 \;,$$

in agreement, within the errors, with the pion values.

The K^-/π^- ratio, on the contrary, does not ap-

pear to scale, although this cannot be completely ruled out because at $x_\perp > 0.45$ the errors could conceivably accommodate parallel curves.

C. Proton and antiproton production

The ratios of p/π^+ and $\bar{p}/\pi^-$ from the W target are plotted in Fig. 13 as a function of $p_\perp$ for the three incident proton energies. As $p_\perp$ decreases from 1.5 GeV/c both ratios decrease and tend to become s-independent. This feature, also observed with kaons, indicates that the invariant cross sections of particles heavier than pions do not rise with decreasing $p_\perp$ as fast as pions in this region. In fact, the $K^\pm$, p, and $\bar{p}$ cross sections plotted against $p_\perp$ fall off almost exponentially all the way from ~1 to 7 GeV/c, the protons showing the smallest s dependence.
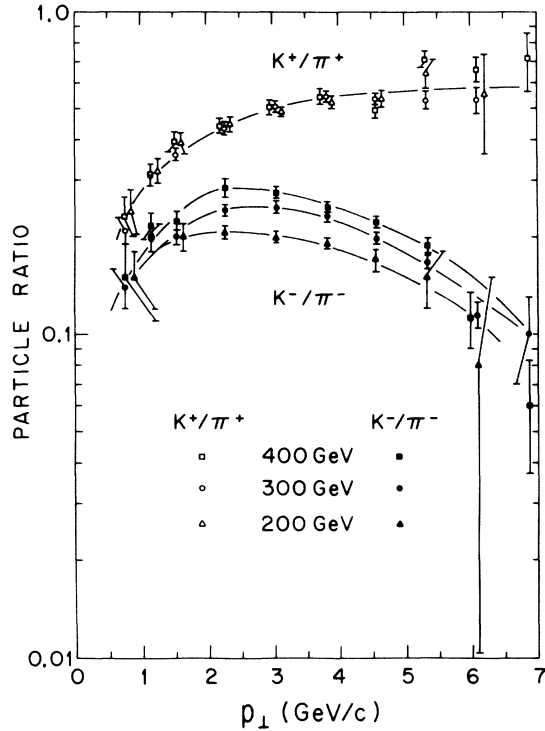
As already mentioned above, the $\bar{p}/\pi^-$ ratio

FIG. 11. Cross-section ratios K^+/π^+ and K^-/π^- versus $p_\perp$ for W target.
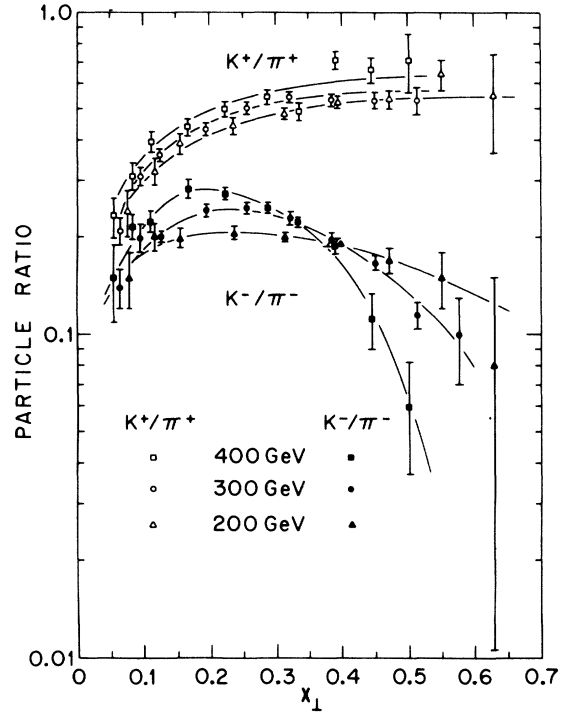

FIG. 12. Cross-section ratios K^+/π^+ and K^-/π^- versus $x_\perp$ for W target.

shows at $p_\perp > 1.5$ GeV/c the same $\sqrt{s}$ dependence at fixed $p_\perp$ as the K^-/π^- ratio, but it falls off faster with increasing $p_\perp$, dropping by a factor of ~10 from $p_\perp = 1.5$ to 6 GeV/c.

When plotted against $x_\perp$, as in Fig. 14, neither the p/π^+ nor the $\bar{p}/\pi^-$ ratio seems to scale as the pions and K^+ do. However, the errors are again sufficiently large, especially in the case of $\bar{p}/\pi^-$, to accommodate nearly parallel curves at $x_\perp > 0.45$.

D. Deuteron and antideuteron production

The d/π^+ and $\bar{d}/\pi^-$ ratios from the W target are displayed in Fig. 13. These were measured only for 300-GeV incident protons.

A direct comparison of our $\bar{d}$ cross sections with data obtained at the ISR[15] and Fermilab[16] is difficult because they were measured under quite different conditions. At 300 GeV Appel *et al.*[16] obtained with a W target and in the forward direction ($p_\perp = 0$) at 30-GeV/c lab momentum, a ratio $\bar{d}/\pi^- \approx 10^{-5}$. At the ISR the British-Scandinavian Collaboration[15] observed $\bar{d}/\pi^- = 5 \times 10^{-5}$ at $p_\perp = 0.7$ GeV/c and $\sqrt{s} = 53$ GeV. We observe $\bar{d}/\pi^- 1.4 \times 10^{-4}$ at $p_\perp = 2.3$ GeV/c. This large relative yield seems to confirm what had already been apparent with $\bar{p}$ production, namely that heavy particles are more copiously produced relative
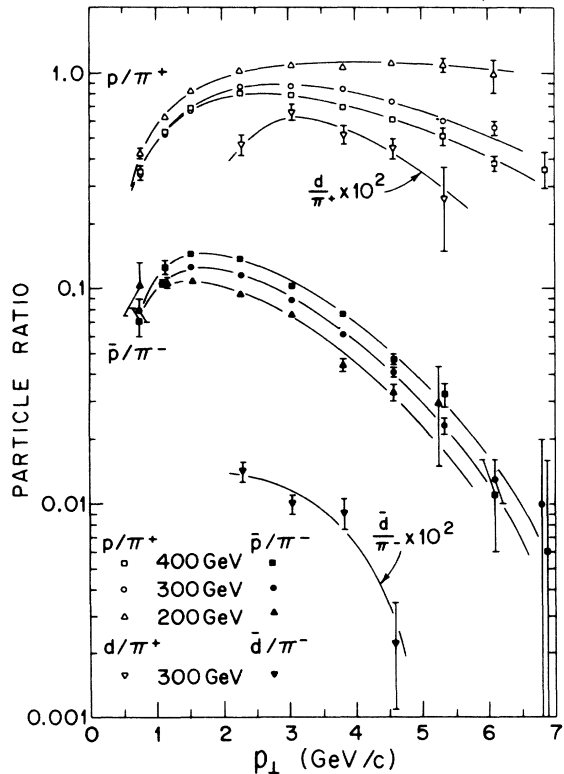

FIG. 13. Cross-section ratios p/π^+, $\bar{p}/\pi^-$, d/π^+, and $\bar{d}/\pi^-$ versus $p_\perp$ for W target.

to pions at high $p_\perp$. However, heavy antiparticle production falls off faster with increasing $p_\perp$ than their counterpart. This feature is illustrated in Fig. 15.

Many models[17-20] have been proposed and tested to explain deuteron (and antideuteron) formation at lower energies. A mechanism which seems to account roughly for the observed rates involves the pairing of a neutron (antineutron) and a proton (antiproton) of approximately equal momenta. The characteristic of all these models is that they provide a connection between the number of deuterons (antideuterons) emerging at a given angle and momentum, and the corresponding number of protons (antiprotons) at the angle but at *half* that momentum. A direct consequence of such models, already put to a test when antideuterons were first observed,[20] is the following relation:

$$\frac{d}{\bar{d}} (p') \cong \left[\frac{p}{\bar{p}} (p'/2) \right]^2 ,$$

where p' is the emerging deuteron (antideuteron) momentum. It is clear from Fig. 15 that such a relation is reasonably well satisfied, within the errors, by our 300-GeV data.

E. Dependence of invariant cross section on atomic number

The effective number of nucleons, $A_{\rm eff} = \sigma_{\rm abs}/\sigma_p$, first used to reduce the W data above to cross sections for a nucleus with atomic number $A = 1$ corresponds approximately to an $A^{0.71}$ dependence. However, the data presented in Tables V–VIII for 300-GeV protons incident on Be, Ti, and W targets indicate a variation of the cross section with A which is much stronger, in general, than $A^{0.71}$.

We have parametrized the A dependence of the invariant cross section per nucleus by

$$I_i(p_\perp, A) = I_i(p_\perp, 1) A^{\alpha_i(p_\perp)},$$

where we have abbreviated the invariant cross section $E d\sigma/d^3p$ by I. For each particle species i and each value of $p_\perp$ we have made a least-squares fit to the Be, Ti, and W cross sections to the above formula in order to extract $\alpha_i(p_\perp)$ and $I_i(P_\perp, 1)$. In every case the data gave a reasonably good fit. For pions the average χ^2 was 0.9 for one degree of freedom. For kaons and protons the average χ^2 was somewhat worse—1.6 for one degree of freedom. Figure 16 shows a typical atomic number

FIG. 14. Cross-section ratios p/π^+ and $\bar{p}/\pi^-$ versus $x_\perp$ for W target.
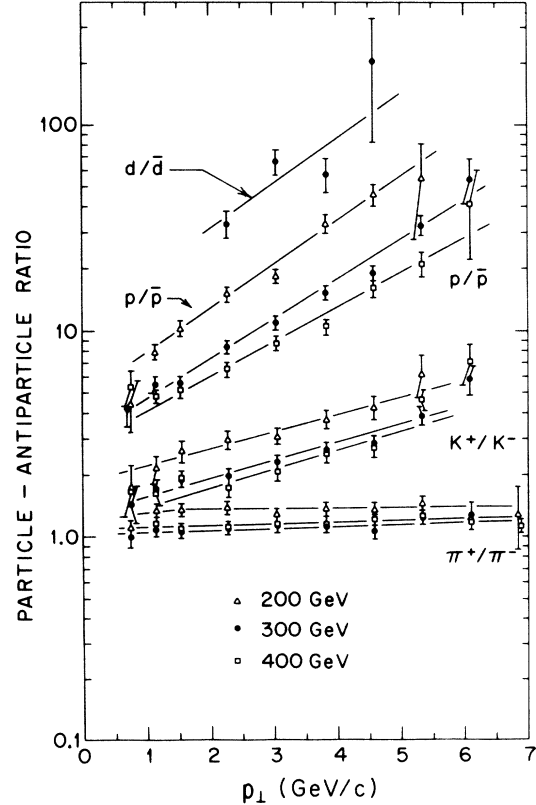

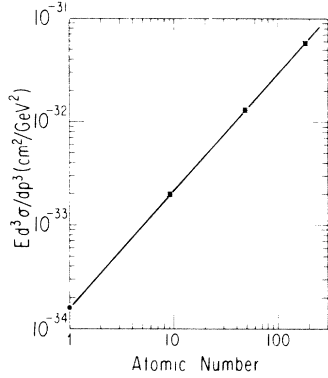FIG. 15. Particle-antiparticle ratios versus $p_\perp$ for W target.

FIG. 16. Extrapolation to the cross section for a nucleus with $A = 1$ from measured proton-nucleus cross sections on Be, Ti, and W. (The data refer to π^- production at $p_\perp = 4.58$ GeV/c by 300-GeV protons.)

FIG. 17. Plots of the power α of the A dependence versus $p_\perp$ for the production of hadrons by 300-GeV protons; (a) π^+, (b) π^-, (c) K^+, (d) K^-, (e) p, and (f) $\bar{p}$.

dependence for π^- production at $p_\perp = 4.58$ GeV/c by 300-GeV incident protons.

In Fig. 17 the exponent α is plotted vs $p_\perp$ for each particle species. At low $p_\perp$ the exponent approaches the expected $A^{0.71}$ behavior, while at high $p_\perp$ the exponent rises above unity. For π^+ the exponent becomes constant at 1.12 for $p_\perp \geq 3.5$ GeV/c, and there are indications that a similar behavior obtains for K^+, p, and $\bar{p}$ with even larger values of the exponent.

We should emphasize that the power α is significantly larger than unity. This means that the nucleons in the nucleus are behaving in a *cooperative* fashion. (If the nucleons all acted independently and there were no shielding effects, one would expect the cross section to be proportional to A.) These effects observed in the proton-nucleus collisions are not understood at present.

The other quantity extracted from the fit, $I_i(p_\perp, 1)$, is the invariant cross section for a nucleus with $A = 1$, where the effective nucleon is an average between neutrons and protons typical of the nuclei measured. The quantity $A^{\alpha_i(p_\perp)}$ is the effective number of nucleons. Since measurements were made on three nuclei only for 300-GeV incident protons, the cross sections for $A = 1$ cannot be extracted for 200 GeV and 400 GeV without an additional assumption. We assume that the effective number of nucleons depends only on the $p_\perp$ and species of the *outgoing* particle, and does not depend on the incident proton energy. Thus we assume $A_{\text{eff}} = A^{\alpha_i(p_\perp)}$ for all three energies.

In Table IX we present the cross sections extrapolated to $A = 1$ for π^+ and π^- for 200-, 300-, and 400-GeV incident protons. The errors stated are only the errors of extrapolation and include no consideration of a possible incorrect param-
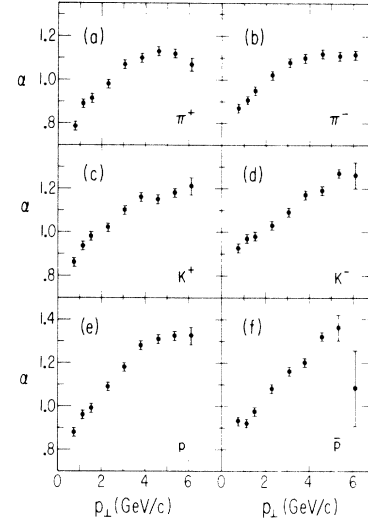
etrization at low atomic number. In Table X we present the ratio of cross sections extrapolated to $A = 1$ for "K/π" as a function of $p_\perp$. (The quotation marks denote the ratio extrapolated to $A = 1$.) In Table XI we present the ratio "p/π" in the same format.

In Fig. 18 we plot the π^- cross sections extrapolated to $A = 1$ against $x_\perp$ for the three energies. One again sees that the lines are parallel for $x_\perp > 0.4$, indicating that the scaling form

$$I \propto (\sqrt{s})^{-n} e^{-a x_\perp}$$

still holds with $n = 10.5 \pm 0.4$ and $a = 35.2 \pm 0.4$. This result shows that the basic scaling behavior observed in the W collisions is not altered by the extrapolation to cross sections for $A = 1$ discussed above.

F. Comparison with other measurements

In Fig. 19 we compare our results extrapolated to $A = 1$ for π^- at $\sqrt{s} = 23.7$ GeV with measurements made at the ISR at $\sqrt{s} = 23.4$ GeV of π^- by the Saclay-Strasbourg collaboration[21] and the British-Scandinavian collaboration,[5,22,23] and of π^0 by the CERN-Columbia-Rockefeller collaboration.[4] The published cross sections of the latter group have all been multiplied by a factor of 0.7 to account for a more precise absolute normalization now available in that experiment.[24] The agreement in shape and absolute value of the points is very good; our data on the average are about 10% higher than the ISR data. When extrapolated to $A = 1$ we find the ratio of cross sections $\pi^+/\pi^- \sim 1.23$ for

TABLE IX. Invariant cross section per effective nucleon for $\pi^{\pm}$ mesons. The method of derivation of this cross section and its errors is discussed in the text. At each $p_{\perp}$ value the top line refers to π^{+} and the bottom line to π^{-}.

$p_{\perp}$ (GeV/c)	$E d\sigma(\pi^{\pm})/d^3p$ (cm^2 GeV^{-2})		
	200 GeV	300 GeV	400 GeV
0.76	$(1.64 \pm 0.16) \times 10^{-27}$	$(1.83 \pm 0.18) \times 10^{-27}$	$(2.17 \pm 0.22) \times 10^{-27}$
	$(1.42 \pm 0.14) \times 10^{-27}$	$(1.75 \pm 0.18) \times 10^{-27}$	$(1.88 \pm 0.19) \times 10^{-27}$
1.14	$(2.48 \pm 0.25) \times 10^{-28}$	$(2.59 \pm 0.26) \times 10^{-28}$	$(2.63 \pm 0.26) \times 10^{-28}$
	$(1.60 \pm 0.16) \times 10^{-28}$	$(2.06 \pm 0.21) \times 10^{-28}$	$(2.00 \pm 0.20) \times 10^{-28}$
1.53	$(3.52 \pm 0.35) \times 10^{-29}$	$(3.65 \pm 0.36) \times 10^{-29}$	$(3.88 \pm 0.39) \times 10^{-29}$
	$(2.12 \pm 0.21) \times 10^{-29}$	$(2.83 \pm 0.28) \times 10^{-29}$	$(2.90 \pm 0.29) \times 10^{-29}$
2.29	$(1.02 \pm 0.10) \times 10^{-30}$	$(1.18 \pm 0.12) \times 10^{-30}$	$(1.30 \pm 0.13) \times 10^{-30}$
	$(0.63 \pm 0.06) \times 10^{-30}$	$(0.93 \pm 0.09) \times 10^{-30}$	$(1.01 \pm 0.10) \times 10^{-30}$
3.05	$(3.22 \pm 0.32) \times 10^{-32}$	$(4.55 \pm 0.46) \times 10^{-32}$	$(5.79 \pm 0.58) \times 10^{-32}$
	$(2.37 \pm 0.24) \times 10^{-32}$	$(3.84 \pm 0.38) \times 10^{-32}$	$(4.82 \pm 0.48) \times 10^{-32}$
3.82	$(1.60 \pm 0.16) \times 10^{-33}$	$(3.04 \pm 0.30) \times 10^{-33}$	$(3.98 \pm 0.40) \times 10^{-33}$
	$(1.03 \pm 0.10) \times 10^{-33}$	$(2.39 \pm 0.24) \times 10^{-33}$	$(3.03 \pm 0.30) \times 10^{-33}$
4.58	$(7.52 \pm 0.75) \times 10^{-35}$	$(1.83 \pm 0.18) \times 10^{-34}$	$(3.06 \pm 0.31) \times 10^{-34}$
	$(5.56 \pm 0.56) \times 10^{-35}$	$(1.65 \pm 0.17) \times 10^{-34}$	$(2.50 \pm 0.25) \times 10^{-34}$
5.34	$(4.25 \pm 0.42) \times 10^{-36}$	$(1.72 \pm 0.17) \times 10^{-35}$	$(2.78 \pm 0.28) \times 10^{-35}$
	$(2.89 \pm 0.29) \times 10^{-36}$	$(1.37 \pm 0.14) \times 10^{-35}$	$(2.24 \pm 0.22) \times 10^{-35}$
6.10	$(3.5 \pm 0.5) \times 10^{-37}$	$(2.57 \pm 0.31) \times 10^{-36}$	$(5.56 \pm 0.66) \times 10^{-36}$
	$(1.7 \pm 0.2) \times 10^{-37}$	$(1.26 \pm 0.13) \times 10^{-36}$	$(2.85 \pm 0.29) \times 10^{-36}$

TABLE X. "K^{+}/π^{+}" (top line) and "K^{-}/π^{-}" (bottom line) cross section ratios extrapolated to $A = 1$.

$p_{\perp}$ (GeV/c)	Particle ratio "$K^{\pm}/\pi^{\pm}$"		
	200 GeV	300 GeV	400 GeV
0.76	0.17 ± 0.02	0.15 ± 0.02	0.16 ± 0.02
	0.11 ± 0.01	0.10 ± 0.01	0.11 ± 0.01
1.14	0.25 ± 0.03	0.24 ± 0.03	0.24 ± 0.03
	0.15 ± 0.02	0.15 ± 0.02	0.16 ± 0.02
1.53	0.29 ± 0.03	0.27 ± 0.03	0.30 ± 0.03
	0.18 ± 0.02	0.18 ± 0.02	0.20 ± 0.02
2.29	0.37 ± 0.04	0.36 ± 0.04	0.37 ± 0.04
	0.19 ± 0.02	0.23 ± 0.02	0.26 ± 0.03
3.05	0.40 ± 0.04	0.42 ± 0.04	0.41 ± 0.04
	0.19 ± 0.02	0.24 ± 0.02	0.26 ± 0.03
3.81	0.40 ± 0.04	0.42 ± 0.04	0.42 ± 0.04
	0.14 ± 0.01	0.16 ± 0.02	0.18 ± 0.02
4.58	0.50 ± 0.05	0.50 ± 0.05	0.46 ± 0.05
	0.11 ± 0.01	0.13 ± 0.01	0.15 ± 0.02
5.34	0.51 ± 0.05	0.42 ± 0.04	0.56 ± 0.06
	0.063 ± 0.006	0.070 ± 0.007	0.079 ± 0.008
6.10	0.34 ± 0.12	0.33 ± 0.07	0.41 ± 0.08
	0.040 ± 0.008	0.058 ± 0.006	0.057 ± 0.006

TABLE XI. "p/π^{+}" (top line) and "$\bar{p}/\pi^{-}$" (bottom line) cross-section ratios extrapolated to $A = 1$.

| $p_{\perp}$ (GeV/c)	Particle ratio "p/π"		
	200 GeV	300 GeV	400 GeV
0.76	0.27 ± 0.04	0.21 ± 0.03	0.22 ± 0.03
	0.072 ± 0.010	0.055 ± 0.008	0.048 ± 0.005
1.14	0.42 ± 0.04	0.36 ± 0.04	0.35 ± 0.04
	0.097 ± 0.010	0.095 ± 0.010	0.115 ± 0.012
1.53	0.59 ± 0.06	0.47 ± 0.05	0.48 ± 0.05
	0.097 ± 0.010	0.112 ± 0.012	0.130 ± 0.013
2.29	0.57 ± 0.06	0.47 ± 0.05	0.44 ± 0.04
	0.073 ± 0.007	0.088 ± 0.009	0.107 ± 0.011
3.05	0.57 ± 0.06	0.45 ± 0.05	0.41 ± 0.04
	0.052 ± 0.006	0.061 ± 0.006	0.069 ± 0.007
3.81	0.43 ± 0.04	0.33 ± 0.03	0.28 ± 0.03
	0.026 ± 0.003	0.036 ± 0.004	0.045 ± 0.005
4.58	0.42 ± 0.04	0.28 ± 0.03	0.23 ± 0.02
	0.012 ± 0.001	0.016 ± 0.002	0.018 ± 0.002
5.34	0.37 ± 0.04	0.21 ± 0.02	0.19 ± 0.02
	0.007 ± 0.003	0.006 ± 0.001	0.008 ± 0.003
6.10	0.29 ± 0.06	0.16 ± 0.03	0.11 ± 0.02
		0.014 ± 0.004	0.012 ± 0.006
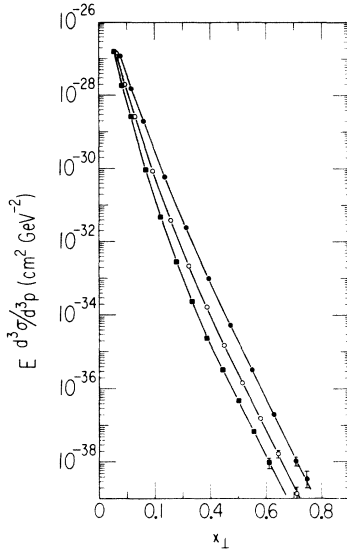
FIG. 18. π^- production cross section extrapolated to $A = 1$ plotted against $x_\perp$. Measurements at incident proton energies of 200, 300, and 400 GeV are indicated by closed circles, open circles, and closed squares, respectively.
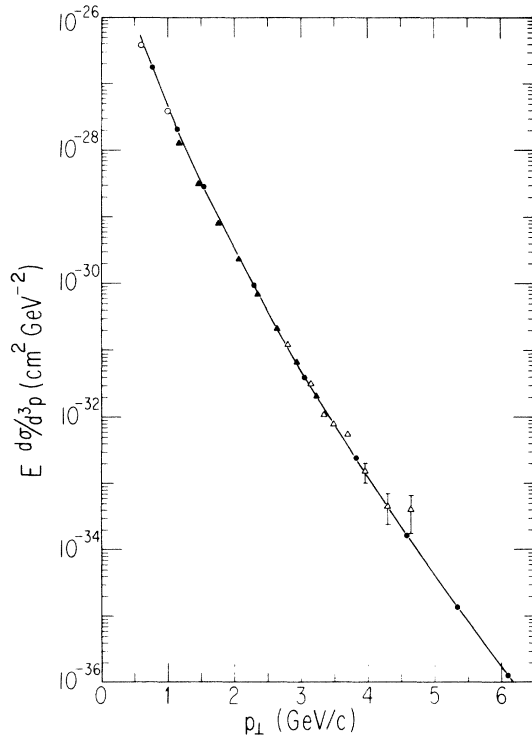

FIG. 19. Comparison of the π^0 and π^- cross sections obtained at the CERN ISR, with π^- cross sections extrapolated to $A = 1$ in this experiment. Data were obtained from the following references: open circles, Ref. 21; closed triangles, Ref. 23; open triangles, Ref. 4; closed circles, this experiment.
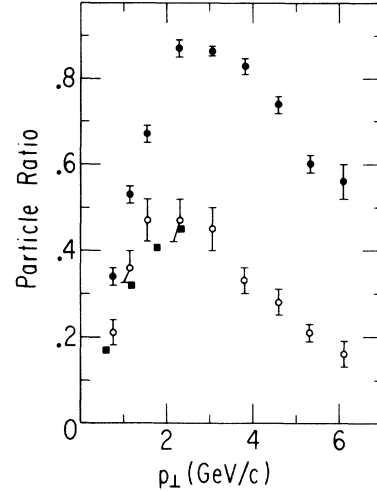
FIG. 20. Comparison of the cross-section ratio p/π^+ measured on tungsten at $\sqrt{s} = 23.7$ GeV (closed circles), with that obtained by extrapolation to $A = 1$ (open circles). Ratios obtained from the British-Scandinavian collaboration (Ref. 23) at $\sqrt{s} = 23.4$ GeV are also plotted (closed squares).

$1.0 < p_\perp < 3.0$ GeV, while the British-Scandinavian collaboration finds a ratio ~ 1.15.[23]

The particle ratios are also sensitive to the extrapolation to $A = 1$ since the A dependence is stronger for heavier particles. Figure 20 shows the extreme case where the ratio p/π^+ measured on the W target for 300-GeV incident protons is compared with the ratio "p/π^+" extrapolated to $A = 1$. We also plot the ratio of cross sections p/π^+ obtained by the British-Scandinavian group at $\sqrt{s} = 23.4$ GeV and 90° c.m. for comparison. These latter ratios were obtained from fits to the cross sections given in their paper. The agreement is quite good. It must be noted that while the British-Scandinavian measurements were made at a fixed angle of 90° in the c.m. system, our measurements were made at a fixed lab angle which, for protons, changes from 135° to 95° in the c.m. system over the range of comparison. Figure 21 shows a similar plot for K^-/π^-. Here the agreement is not as good, but is still reasonable.

The above comparisons between our cross sections extrapolated to $A = 1$ and cross sections from the ISR show good agreement where the data overlap. This agreement gives us confidence that to better than 20% accuracy, the extrapolation procedure can give cross sections which would be obtained in actual nucleon-nucleon collisions. It is then interesting to make a comparison of inclusive pion production in the region of 90° c.m. over as wide a range of kinematic variables as possible. All the readily available data for π^- and π^0 pro-

duction at 90° c.m. have been plotted on a single graph. The data span the range from $\sqrt{s}$ =4.7 GeV to 63 GeV. As noted above, most theories predict in their regions of applicability that the form of the invariant cross section at 90° is given by

$$I = (\sqrt{s}\,)^{-n} f(x_\perp) .$$

This expression is equivalent to an alternate expression

$$I = p_\perp^{-n} g(x_\perp) ,$$

with the same exponent n. The value of the exponent is one characteristic which distinguishes various theories. For example, $n = 4$ is characteristic of a theory in which the high $p_\perp$ processes are dominated by gluon exchange between elementary constituents[6, 25, 26] $n = 8$ is characteristic of the constituent interchange model in its most elementary form.[27]

We have plotted in Fig. 22 $\ln I$ against $\ln\sqrt{s}$ for fixed $x_\perp$. The slope $[\partial(\ln I)/\partial(\ln\sqrt{s}\,)]_{x_\perp}$ is equal to $-n$ and hence gives the local value of n in any region of $\sqrt{s}$ for any region of $x_\perp$.

In the ISR range, data were obtained from the CERN-Columbia-Rockefeller collaboration,[4] the British-Scandinavian collaboration,[23] and the Saclay-Strasbourg collaboration.[3, 21] In the lower energy range, data on π^- inclusive production at ~90° c.m. were obtained from Blobel et al.,[28] Akerlof et al.,[29] Amaldi et al.,[30] and the French-Soviet collaboration using the Mirabelle bubble chamber.[31] In the Fermilab energy region, data for π^- production at ~90° c.m. from this experiment, and data for π^0 production from Carey et al.,[32] are plotted. The data from our experiment are the cross sections extrapolated to $A = 1$ as discussed above. By examination of Fig. 22 some general features can be discerned. The data show a smooth variation over the entire energy region, with no evidence of the onset of a threshold. One should note, however, the paucity of data between $\sqrt{s}$ = 6.8 GeV and 23.7 GeV, a region where some threshold might exist.

The agreement between the various experiments is remarkably good. There does not appear to be any distinct scaling region. As $x_\perp$ increases, the local value of n increases almost monotonically. Figure 23 shows the value of n obtained for large $\sqrt{s}$ from Fig. 22 as a function of $x_\perp$. For $x_\perp = 0.2$, which is the centroid of the ISR data, $n \approx 8$. In the region where this experiment overlaps the ISR, the local exponent is 8. At larger $x_\perp$, $n \approx 11$.

In Fig. 22 we have also plotted curves of cross section for fixed $p_\perp$. The cross section for a given $p_\perp$ rises sharply from threshold (indicated by the dashed lines) and flattens out as the energy becomes large compared to the threshold. If one roughly extrapolates the cross sections for fixed
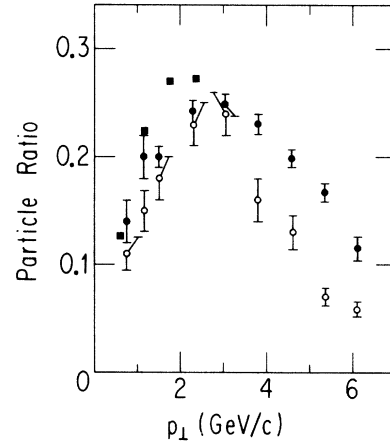

FIG. 21. Comparison of the cross-section ratio K^-/π^- measured on tungsten at $\sqrt{s}$ =23.7 GeV (closed circles), with that obtained by extrapolation to A =1 (open circles). Ratios obtained from the British-Scandinavian collaboration (Ref. 23) at $\sqrt{s}$ =23.4 GeV are also plotted (closed squares).
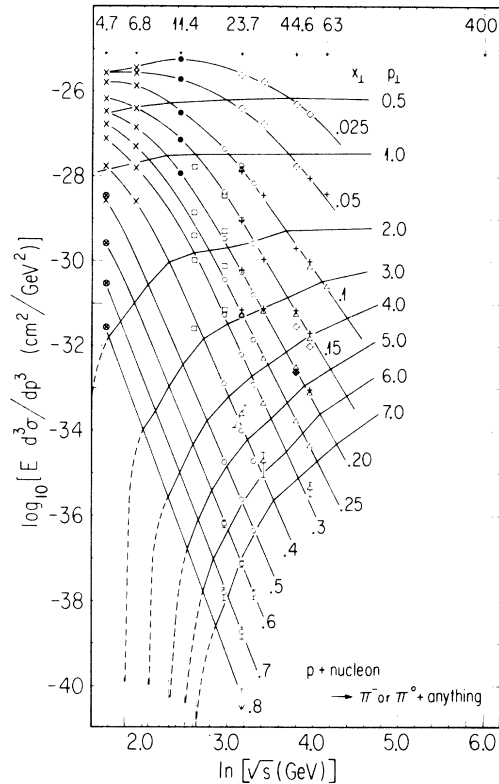

FIG. 22. Global plot of invariant cross sections for inclusive π^- and π^0 production at 90° c.m. (see text). Data were obtained from the following references: open squares, Ref. 32; open triangles, Ref. 4; vertical crosses, Ref. 23; open diamonds, Refs. 3 and 21; open circles, this experiment; crosses, Ref. 28; closed circles, Ref. 31; crossed circles, Ref. 29. Cross sections are plotted for constant values of $x_\perp$; lines of cross section for fixed $p_\perp$ as a function of $\ln\sqrt{s}$ are also shown.

$p_\perp$ to very high energy, one finds a cross section which goes as $1/p_\perp^{~6}$, independent of $\sqrt{s}$. This behavior is Feynman-scaling.

Even without a specific theory, the general features of high-$p_\perp$ phenomena are hardly surprising. The often quoted restriction of high $p_\perp$ (see Ref. 33) before the ISR and the Fermilab data became available can be understood as the suppression of the cross section near the threshold. As $\sqrt{s}$ increases, a given $p_\perp$ is further above threshold and the corresponding cross section rises to some limiting value when $p_\perp$ is small compared to $\sqrt{s}$ (i.e., $x_\perp \to 0$). There appears to be a gentle spreading of the Feynman-scaling region out to ever larger $p_\perp$ as the energy increases. This behavior seems quite natural, and, in retrospect, the surprise at the violation of the $e^{-6p_\perp}$ dependence found at lower energies seems unjustified. Of course, the manner in which the Feynman scaling is approached and the limiting form of the $p_\perp$ distribution at large $\sqrt{s}$ should be understood. Such understanding might involve consideration of the internal structure of the nucleon.

In Fig. 24 we present a similar global plot for inclusive proton production. Again, continuity over the entire energy range is consistent with the available data. The general features are the same as the plot for pions except for small $\sqrt{s}$, where the effect of the presence of the proton in the initial state is evident.

For the process $p + p \to p +$anything, the limiting process for $x_\perp = 1$ is elastic scattering. We have also plotted the differential cross section $d\sigma/dt$ for p-p scattering at 90° c.m.[34] in Fig. 24. While data for intervening values of $x_\perp$ are missing, the s dependence of the elastic cross section corresponds quite well with the limiting exponent n, as deduced from the variation of n with $x_\perp$ for inclusive proton production. Figure 25 shows the exponent n versus $x_\perp$ and the value for elastic scattering to demonstrate the point.
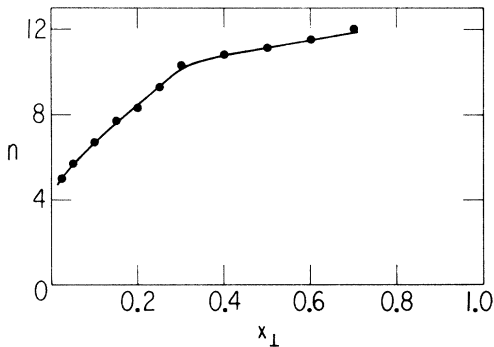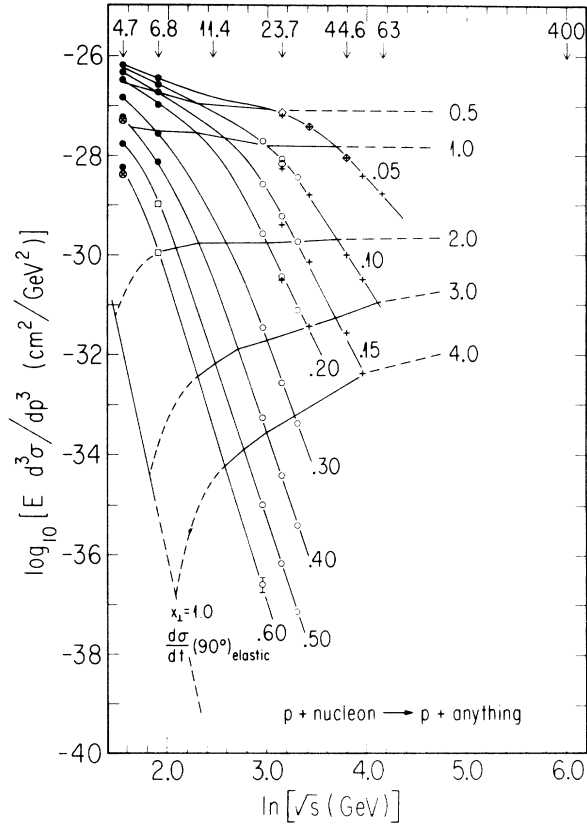

FIG. 24. Global plot of invariant cross sections for inclusive proton production at 90° c.m. (see text). Data were obtained from the following references: vertical crosses, Ref. 23; open diamonds, Refs. 3 and 21; open circles, this experiment; closed circles, Ref. 28; crossed circles, Ref. 29; open squares, Ref. 30. Elastic scattering line was obtained from Ref. 34.

VII. SUMMARY AND CONCLUSIONS

In this paper we have presented the results of an experimental study of the production of hadrons at ~90° c.m. by incident protons of 200, 300, and

FIG. 23. Plot of exponent n (see text) versus $x_\perp$ for inclusive pion production at large $\sqrt{s}$.
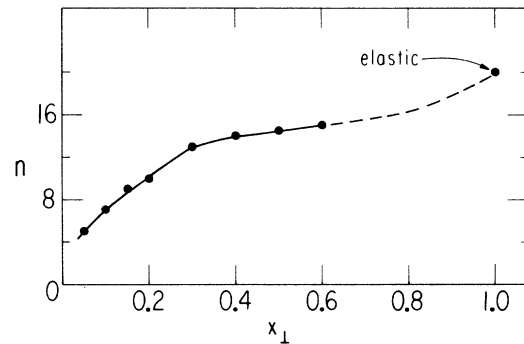

FIG. 25. Plot of exponent n (see text) versus $x_\perp$ for inclusive proton production.

400 GeV on nuclear targets. The invariant cross sections for the inclusive production of $\pi^{\pm}$, $K^{\pm}$, and $\bar{p}$ show a dependence on incident proton energy which becomes stronger as the transverse momentum of the observed particle increases. The production of protons shows only a small energy dependence.

The cross sections for $\pi^{\pm}$ and K^{+} fit a scaling form $E d\sigma/d^3p = (\sqrt{s})^{-n}f(x_{\perp})$ for $x_{\perp} > 0.4$ with $n \approx 11$. However, when the cross sections found in this experiment are compared with all the available data, over a wide range of $\sqrt{s}$ and $x_{\perp}$, no distinct scaling region appears.

The cross sections show a very strong A dependence at high $p_{\perp}$. While the atomic number dependence is close to $A^{0.71}$ at low $p_{\perp}$, the dependence becomes, at high $p_{\perp}$ (> 4 GeV/c), $A^{1.1}$ for pion production, and $A^{1.3}$ for proton and antiproton production. The nucleons in the nucleus appear to act collectively in the production of high-$p_{\perp}$ hadrons.

There does not appear to be any theory of high-$p_{\perp}$ particle production which fits these observations in a convincing fashion.

ACKNOWLEDGMENTS

*Work supported by the National Science Foundation and the U. S. Atomic Energy Commission.

[1]See, for example, G. Cocconi, Nuovo Cimento 57A, 837 (1968).

[2]A. Bertin et al., Phys. Lett. 42B, 493 (1972); M. Banner et al., ibid. 41B, 547 (1972).

[3]M. Banner et al., Phys. Lett. 44B, 537 (1973).

[4]F. W. Büsser et al., Phys. Lett. 46B, 471 (1973).

[5]B. Alper et al., Phys. Lett. 44B, 521 (1973); 44B, 527 (1973).

[6]S. M. Berman, J. D. Bjorken, and J. B. Kogut, Phys. Rev. D 4, 3388 (1971).

[7]R. Blankenbecler, S. J. Brodsky, and J. F. Gunion, Phys. Lett. 42B, 461 (1972).

[8]References to the many theoretical papers can be found in J. D. Bjorken, in Proceedings of the 2nd International Conference on Elementary Particles, Aix-en-Provence, 1973 [J. Phys. (Paris) Suppl. 34, C1-1426 (1973)], and P. V. Landshoff, in Proceedings of the XVII International Conference on High Energy Physics, London, 1974, edited by J. R. Smith (Rutherford Laboratory, Chilton, Didcot, Berkshire, England, 1974), p. V-57.

[9]In the calculation of the lengths of the nuclear targets we used the absorption cross sections measured for 20-GeV/c protons incident on nuclei by G. Bellettini et al., Nucl. Phys. 79, 609 (1966).

[10]J. W. Cronin et al., Phys. Rev. Lett. 31, 1426 (1973).

[11]J. P. Boymond et al., Phys. Rev. Lett. 33, 112 (1974).

[12]J. W. Cronin et al., Phys. Rev. D 10, 3093 (1974).

[13]D. C. Carey et al., Phys. Rev. Lett. 32, 24 (1974).

[14]J. A. Appel et al., Phys. Rev. Lett. 33, 719 (1974).

[15]B. Alper et al., Phys. Lett. 46B, 265 (1973).

[16]J. A. Appel et al., Phys. Rev. Lett. 32, 428 (1974).

[17]S. T. Butler and C. A. Pearson, Phys. Rev. Lett. 7, 69 (1961); Phys. Lett. 1, 77 (1962); Phys. Rev. 129,

836 (1963).

[18]A. Schwarzschild and Č. Zupančič, Phys. Rev. 129, 854 (1963).

[19]P. A. Piroué and A. J. S. Smith, Phys. Rev. 148, 1315 (1966).

[20]D. E. Dorfan et al., Phys. Rev. Lett. 14, 1003 (1965).

[21]M. Banner et al., Phys. Lett. 41B, 547 (1972).

[22]B. Alper et al., Phys. Lett. 47B, 75 (1973); 47B, 275 (1973).

[23]B. Alper et al., Nucl. Phys. B87, 19 (1975).

[24]L. DiLella (private communication).

[25]P. V. Landshoff and J. C. Polkinghorne, Phys. Lett. 45B, 361 (1973).

[26]S. D. Ellis and M. B. Kislinger, Phys. Rev. D 9, 2026 (1974).

[27]R. Blankenbecler and S. J. Brodsky, Phys. Rev. D 10, 2973 (1974). This reference presents refinements to the original constituent interchange model of Ref. 7. The dependence of the invariant cross section on the kinematic variables is no longer characterized in such a simple fashion.

[28]V. Blobel et al., Nucl. Phys. B69, 454 (1974).

[29]C. W. Akerlof et al., Phys. Rev. D 3, 645 (1971).

[30]U. Amaldi et al., Nucl. Phys. B86, 403 (1975).

[31]V. A. Bumazshnov et al., Phys. Lett. 50B, 283 (1974).

[32]D. C. Carey et al., Phys. Rev. Lett. 33, 327 (1974); 33, 330 (1974).

[33]For example, in the paper of Berman, Bjorken, and Kogut, Ref. 6, hadron production is extrapolated as $\exp(-6p_{\perp})$.

[34]C. M. Ankenbrandt et al., Phys. Rev. 170, 1223 (1968); J. V. Allaby et al., Phys. Lett. 23, 389 (1966); 25B, 156 (1967); C. W. Akerlof et al., Phys. Rev. 159, 1138 (1967); G. Cocconi et al., ibid. 138, B165 (1965).